AMERICAN SOCIETY FOR MICROBIOLOGY | Journal of Virology®

STRUCTURE AND ASSEMBLY

Cryo-electron Microscopy Structure, Assembly, and Mechanics Show Morphogenesis and Evolution of Human Picobirnavirus

Álvaro Ortega-Esteban,[a] Carlos P. Mata,[a]* María J. Rodríguez-Espinosa,[a] Daniel Luque,[b] Nerea Irigoyen,[a]* Javier M. Rodríguez,[a] Pedro J. de Pablo,[c] José R. Castón[a]

[a]Department of Structure of Macromolecules, Centro Nacional de Biotecnología, Madrid, Spain
[b]Centro Nacional de Microbiología/ISCIII, Majadahonda, Madrid, Spain
[c]Department of Condensed Matter Physics, Universidad Autónoma de Madrid, Madrid, Spain

Álvaro Ortega-Esteban and Carlos P. Mata contributed equally to this work. They are listed in alphabetical order based on first name.

ABSTRACT Despite their diversity, most double-stranded-RNA (dsRNA) viruses share a specialized T=1 capsid built from dimers of a single protein that provides a platform for genome transcription and replication. This ubiquitous capsid remains structurally undisturbed throughout the viral cycle, isolating the genome to avoid triggering host defense mechanisms. Human picobirnavirus (hPBV) is a dsRNA virus frequently associated with gastroenteritis, although its pathogenicity is yet undefined. Here, we report the cryo-electron microscopy (cryo-EM) structure of hPBV at 2.6-Å resolution. The capsid protein (CP) is arranged in a single-shelled, ~380-Å-diameter T=1 capsid with a rough outer surface similar to that of dsRNA mycoviruses. The hPBV capsid is built of 60 quasisymmetric CP dimers (A and B) stabilized by domain swapping, and only the CP-A N-terminal basic region interacts with the packaged nucleic acids. hPBV CP has an α-helical domain with a fold similar to that of fungal partitivirus CP, with many domain insertions in its C-terminal half. In contrast to dsRNA mycoviruses, hPBV has an extracellular life cycle phase like complex reoviruses, which indicates that its own CP probably participates in cell entry. Using an *in vitro* reversible assembly/disassembly system of hPBV, we isolated tetramers as possible assembly intermediates. We used atomic force microscopy to characterize the biophysical properties of hPBV capsids with different cargos (host nucleic acids or proteins) and found that the CP N-terminal segment not only is involved in nucleic acid interaction/packaging but also modulates the mechanical behavior of the capsid in conjunction with the cargo.

IMPORTANCE Despite intensive study, human virus sampling is still sparse, especially for viruses that cause mild or asymptomatic disease. Human picobirnavirus (hPBV) is a double-stranded-RNA virus, broadly dispersed in the human population, but its pathogenicity is uncertain. Here, we report the hPBV structure derived from cryo-electron microscopy (cryo-EM) and reconstruction methods using three capsid protein variants (of different lengths and N-terminal amino acid compositions) that assemble as virus-like particles with distinct properties. The hPBV near-atomic structure reveals a quasisymmetric dimer as the structural subunit and tetramers as possible assembly intermediates that coassemble with nucleic acids. Our structural studies and atomic force microscopy analyses indicate that hPBV capsids are potentially excellent nanocages for gene therapy and targeted drug delivery in humans.

KEYWORDS 3D cryo-EM, capsid protein, dsRNA virus, hPBV, virus assembly

Double-stranded-RNA (dsRNA) viruses infect a diversity of hosts, including bacteria, unicellular and simple eukaryotes (fungi, protozoa), and complex systems (plants and animals). Although capsid complexity ranges from a single shell to multishelled

Citation Ortega-Esteban Á, Mata CP, Rodríguez-Espinosa MJ, Luque D, Irigoyen N, Rodríguez JM, de Pablo PJ, Castón JR. 2020. Cryo-electron microscopy structure, assembly, and mechanics show morphogenesis and evolution of human picobirnavirus. J Virol 94: e01542-20. https://doi.org/10.1128/JVI.01542-20.

Editor Susana López, Instituto de Biotecnologia/UNAM

Address correspondence to José R. Castón, jrcaston@cnb.csic.es.

* Present address: Carlos P. Mata, Astbury Centre for Structural Molecular Biology, School of Molecular and Cellular Biology, Faculty of Biological Sciences, University of Leeds, Leeds, United Kingdom; Nerea Irigoyen, Division of Virology, Department of Pathology, University of Cambridge, Cambridge, United Kingdom.

Received 28 July 2020
Accepted 8 September 2020
Accepted manuscript posted online 16 September 2020
Published 23 November 2020

concentric capsids, most dsRNA viruses have a specialized icosahedral shell with a triangulation number equal to 1 (T=1), formed by 120 subunits with a capsid protein (CP) dimer as the asymmetric unit (1). This common T=1 core organizes the packaged dsRNA genome segment(s) and encloses the RNA-dependent RNA polymerase(s) (RdRp) for genome replication and transcription (2–5). The T=1 capsid of dsRNA viruses remains structurally undisturbed throughout the viral cycle, isolating their genomes and preventing triggering of host defense mechanisms (6, 7), but allows extrusion of freshly synthesized transcripts into the host cytoplasm for translation or incorporation into virion progeny.

The 120-subunit T=1 capsids have been found in members of the families *Reoviridae* (8–11) (which infect higher eukaryotes) and *Picobirnaviridae* (12), in bacteriophages of the family *Cystoviridae* (13, 14), and in mycoviruses of the families *Totiviridae* (which also includes protozoan and metazoan viruses) (15–17), *Partitiviridae* (18, 19), *Megabirnaviridae* (20), *Quadriviridae* (21), and *Chrysoviridae* (22, 23). Birnaviruses are an exception, as they lack the T=1 capsid and have a single T=13 shell (24, 25).

The stoichiometry and conserved architecture of dsRNA virus capsids, built from 60 asymmetric units (CP dimers), provide an optimal platform for the numerous activities related to RNA synthesis. The CP fold is the hallmark of the dsRNA virus lineage, although sequence similarities among CPs are negligible. Structural comparisons based on CP folds indicate that evolution has led to a small number of viral lineages derived from a common ancestor, probably due to capsid assembly constraints (26, 27). Four lineages have been described to date: (i) the picornavirus-like lineage, with a single β-barrel parallel to the capsid surface as the CP fold; (ii) the head-tailed phages and herpesviruses, which share the Hong Kong 97 (HK97)-like CP fold; (iii) viruses with a double β-barrel CP perpendicular to the capsid surface (prototypes are phage PRD1 and adenovirus); and (iv) the dsRNA or bluetongue virus (BTV)-like viruses. In most dsRNA viruses, the capsid subunits nucleate around the genomic single-stranded-RNA (ssRNA) segment(s) as in the picornavirus-like lineage (28–30), with the exception of cystoviruses, which encapsidate ssRNA into a preformed procapsid (13).

Picobirnaviruses (PBV) (31) are detected mainly in stool samples from humans and other vertebrates (32) and in invertebrates (33). The conserved prokaryotic ribosome binding site sequence that precedes each start codon has suggested that PBV are in fact bacteriophages that infect the host intestinal microbiome (34, 35). Given the lack of a suitable cell culture system, current knowledge of PBV biology is very limited. Human PBV (hPBV) pathogenicity is not established; hPBV might be associated with gastroenteritis, but it has also been found in healthy respiratory tracts (36).

Our studies were initiated from a synthetic DNA that spans the whole genome of hPBV strain Hy005102 (37), which consists of two dsRNA segments (~4.3 kbp in total). dsRNA 1 (~2.5 kbp) encodes the CP and a protein of unknown function, and dsRNA 2 (~1.8 kbp) encodes the RdRp (38). The X-ray structure of the rabbit PBV (rPBV) capsid showed that it is based on an ~37-nm-diameter icosahedral T=1 shell formed by 60 symmetric dimers (12); similar quaternary organization was observed in the partitivirus *Penicillium stoloniferum* virus F (PsV-F) (18). Here, we used complementary cryo-EM and biophysical analysis to study capsid structure, assembly, and mechanics of hPBV. The CP N-terminal end faces the capsid interior and is involved in interaction with and packaging of nucleic acids, and it also modulates the mechanical behavior of the hPBV capsid in conjunction with the packaged cargo.

RESULTS

hPBV capsid design and characterization. rPBV capsid structure at 3.4-Å resolution showed that the CP N-terminal ends face the capsid interior (12). Assuming a similar arrangement, we designed three hPBV CP versions that differ in their N-terminal ends and could thus have different inner surfaces and properties: (i) hPBV CP contains the full-length CP sequence (552 residues, 62 kDa); (ii) hPBV Δ45-CP lacks the first 45 N-terminal residues (an Arg/Lys-rich segment; 508 residues, 57 kDa); and (iii) hPBV Ht-CP is the full-length CP with an N-terminal 36-residue tag that includes a 6-His

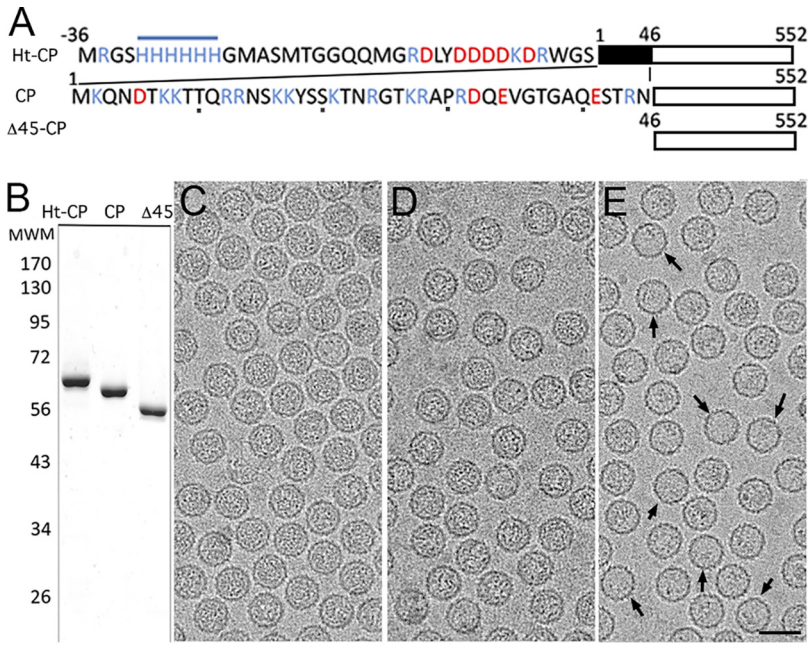

FIG 1 Biochemical and cryo-EM analysis of hPBV CP variants. (A) Scheme of hPBV Ht-CP, CP, and Δ45-CP used, indicating N-terminal sequences and sizes. Acidic residues, red; basic residues, blue. (B) Coomassie blue-stained SDS-PAGE gel of Ht-CP, CP, and Δ45-CP used for cryo-EM data acquisition. Molecular size markers (MWM; Da [10^3]) are on the left. (C to E) Cryo-electron micrographs of Ht-CP (C), CP (D), and Δ45-CP (E) capsids. Arrows (E) indicate empty capsids. Bar, 50 nm.

segment (588 residues, 66.2 kDa) (Fig. 1A). These three CP variants were expressed in *Escherichia coli* at high levels, and the resulting assemblies were purified by ultracentrifugation on a sucrose cushion followed by a linear sucrose gradient. All three CP constructs produced hPBV virus-like particles (VLP) morphologically similar to authentic virions; they were analyzed by negative-staining electron microscopy (EM) (data not shown) and SDS-PAGE (Fig. 1B). In a baculovirus-based expression system, the rPBV CP is processed autoproteolytically after particle assembly and its 65-residue N-terminal end is removed (12), like the Δ45-CP. hPBV CP and Ht-CP were not proteolyzed in the bacterium-based expression system, as reported previously (38). Selected fractions enriched in ~38-nm-diameter VLP were analyzed by cryo-EM in a 300-kV Titan Krios cryo-electron microscope (Fig. 1C to E). Whereas purified Ht-CP and CP VLP were homogeneously full (Fig. 1C and D), Δ45-CP particles were structurally stable (Fig. 1E) with variable internal content (~10% are apparently empty) (Fig. 1E, arrows).

Near-atomic-resolution cryo-EM structure of the hPBV capsid. We calculated icosahedrally averaged maps at 2.63-Å resolution for CP and at 2.8 Å for Δ45-CP and Ht-CP capsids (Fig. 2A), as estimated by the criterion of a 0.143 Fourier shell correlation (FSC) coefficient (Fig. 2B). Using the rPBV CP structure (12) as an initial template, we built three polypeptide chains with Coot (Fig. 2C). Except for differences at the N- and C-terminal regions (see below), the three maps are virtually identical.

The ~380-Å-diameter T=1 capsid showed 60 twisted, elongated protrusions (Fig. 2A, orange), each bearing two copies of CP molecules, one each of A and of B (Fig. 2A; A, blue; B, yellow). The CP dimer, with an almost perfect local 2-fold axis of symmetry, is the asymmetric unit of the capsid. The near-atomic model for CP A and B had 507 and 510 residues, respectively, of the total 552 residues (Fig. 2D; A, rainbow; B, gray). CP A and B lack 42 residues in the N-terminal region, and CP A lacks three C-terminal residues. The CP structure is divided into two domains, a shell (S) and a protruding (P) domain (Fig. 2D, left). In a dimer, the S domains form an ~54- by 115-Å parallelogram and are mostly helical, with a long α helix tangential to the capsid surface (the α3 helix; 39 Å long, 26 residues) (Fig. 2D, right); this long α helix is a common feature of dsRNA

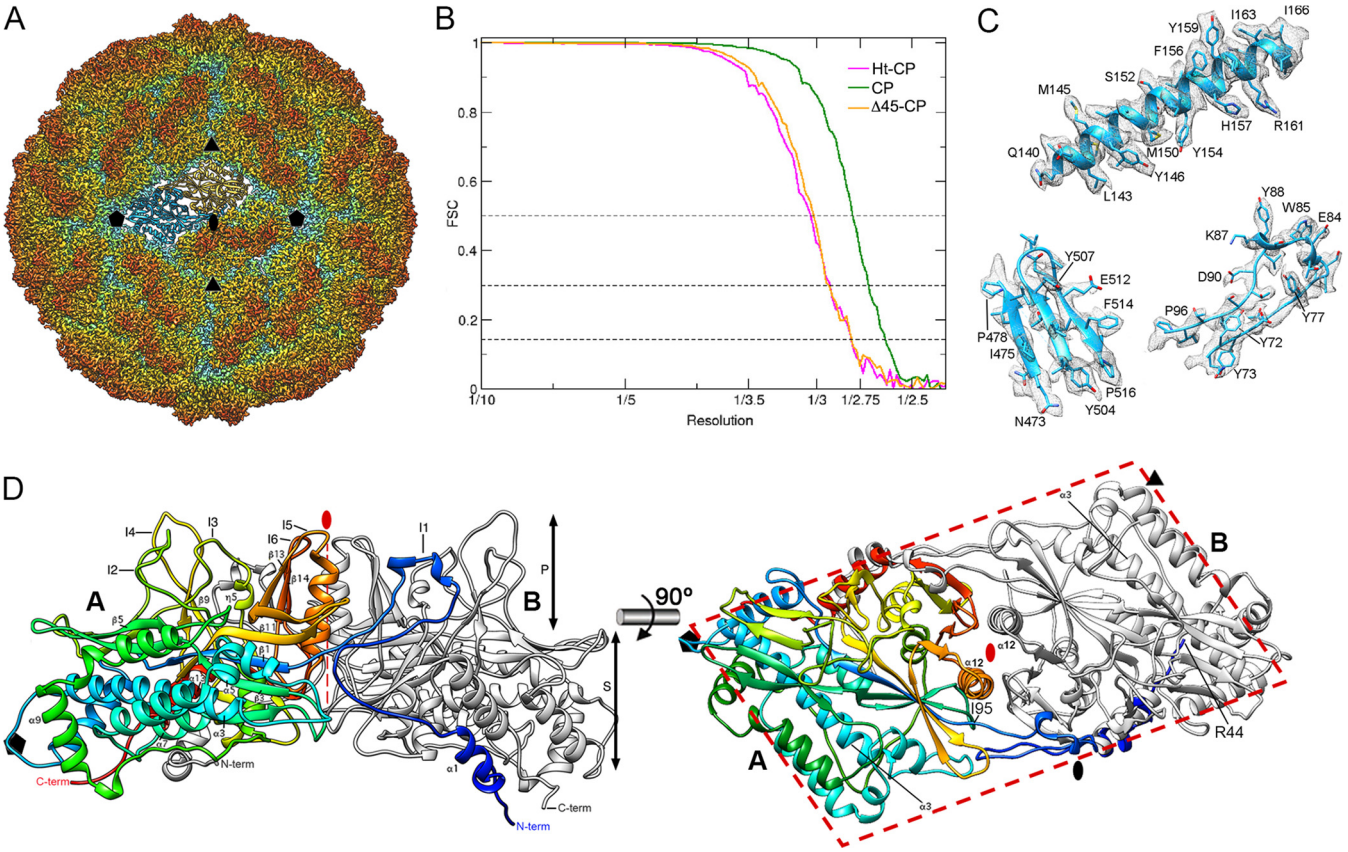

FIG 2 Three-dimensional cryo-EM reconstruction of hPBV capsids at 2.6-Å resolution. (A) Radially color-coded atomic model of hPBV capsid viewed along a 2-fold axis. Protruding dimers (orange) are visible in the T=1 lattice. The atomic structure of a CP dimer of subunits A (blue) and B (yellow) is shown. Symbols indicate icosahedral symmetry axes. (B) Fourier shell correlation (FSC) resolution curve for hPBV. Resolutions based on the 0.5, 0.3, and 0.143 criteria are indicated. For the 0.143 threshold, values for the CP capsid were at 2.63 Å and those for Δ45-CP and Ht-CP capsids were at 2.8 Å. (C) Regions of the cryo-EM density map (gray mesh), with atomic models of helix α3 (residues 140 to 166), a β sheet (residues 473 to 478 and 503 to 516), and a loop (residues 73 to 96). Atomic models are shown as ribbons and sticks, with amino acid residues labeled. (D) Ribbon diagram of the CP dimer (side view, left; top view, right). The A subunit is rainbow-colored from blue (N terminus [N-term]) to red (C terminus [C-term]); the B subunit is in gray. CP domains are indicated (S, shell; P, protruding). The thick dashed line highlights the parallelogram shape. Black symbols indicate icosahedral symmetry axes; the red oval and thin dashed line indicate the local 2-fold symmetry axis.

virus lineage CP. The P domain is built of five ~20-residue insertions in the S domain, made up mainly of β strands (I1 to I4 and I6), and an ~40-residue α/β insertion, with the α12 helix (Fig. 2D, right) perpendicular to the capsid surface around the local quasi-2-fold axis of symmetry (I5) (Fig. 2D, left, I1 to I6; Fig. 3A, colored boxes).

Rabbit and human PBV CP shared substantial similarity. Structural alignment between these two CP using the Dali server (39) (http://ekhidna2.biocenter.helsinki.fi/dali/) showed high structural similarity, with a root mean square deviation (RMSD) of 3.1 Å for 468 aligned residues (z-score = 37.3) (Fig. 3B). Major differences were found in the exposed P domain, which might be involved in interaction with a receptor specific for each species.

The R44-I95 N-terminal segment, involved in a molecular swap between A and B subunits, is responsible for stabilizing the dimer at the S and P domains (Fig. 4). The buried intradimeric interface between A and B subunits is 5,107 Å^2 (calculated with the PISA server; https://pdbe.org/pisa/); removal of this N-terminal segment results in a buried interface of 1,514 Å^2 (Fig. 4A and B). This strong interaction suggested that the CP dimer is the basic precursor assembly.

Structural comparison of hPBV and PsV-F CP. PsV-F and PBV have similar capsid architecture built from quasisymmetric dimers (18, 40), but a detailed structural comparison is lacking. Structural alignment between hPBV and PsV-F CP using the Dali server showed an RMSD of 4.3 Å for 185 residues of 379 (z-score, 5.1), which indicates

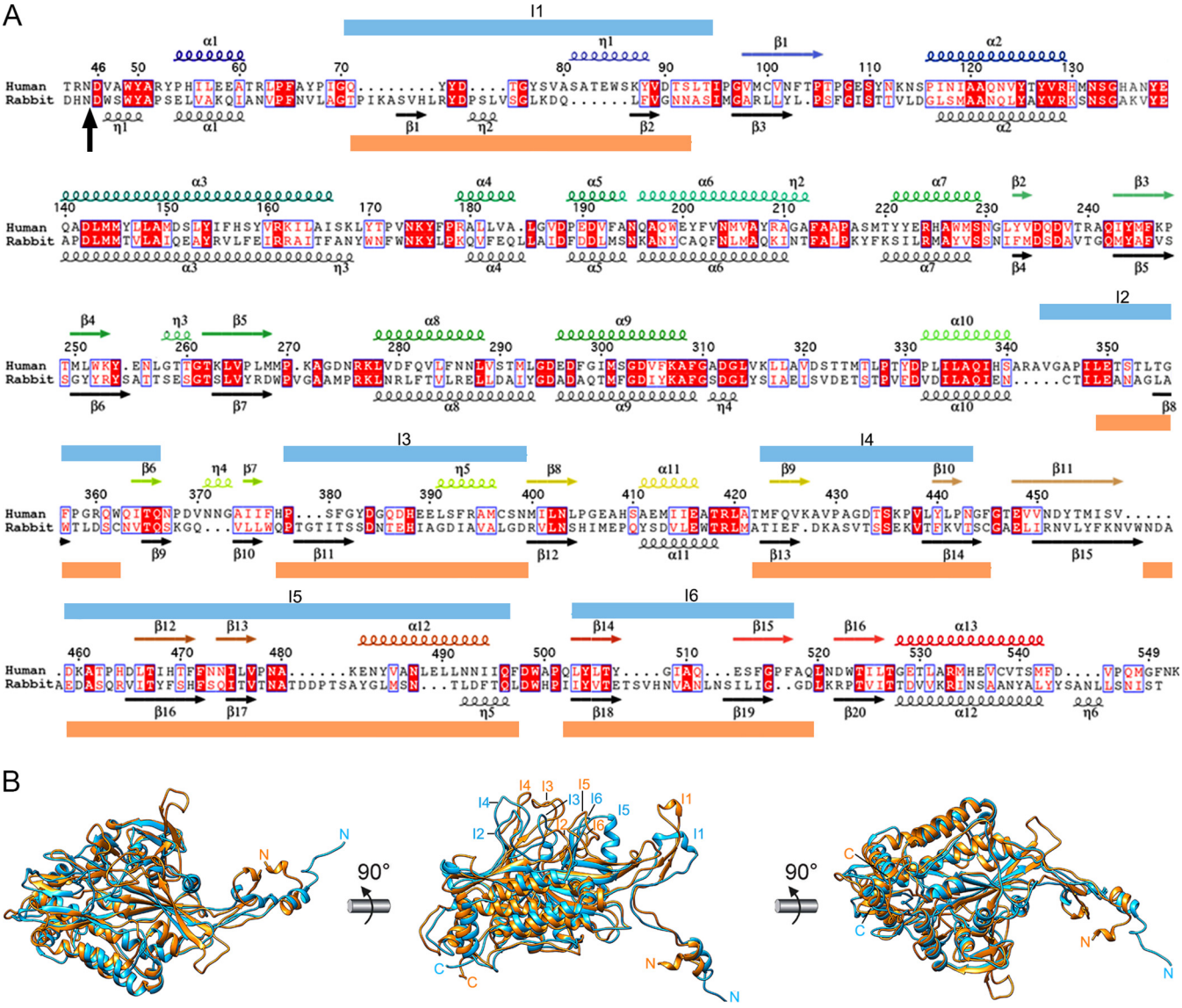

FIG 3 Structural homology of hPBV and rPBV CP. (A) Sequence and secondary structure elements of CP-A, rainbow-colored from blue (N terminus [N-term]) to red (C terminus [C-term]). The N-terminal 42-residue segment is not visible; the aligned sequence and secondary structure elements are shown for rPBV (black). A vertical black arrow indicates the scissile bond in rPBV CP; blue and orange boxes indicate insertions in human and rabbit CP, respectively (I1 to I6). (B) Superimposed rabbit (orange) and human (blue) CP monomers.

a common fold. This fold includes seven α-helices and three β-chains that form a β sheet, all in the S domain (Fig. 5A and 4B). PBV and partitiviruses appear to be closely related and probably share a unique common ancestor. The most similar segments between hPBV and PsV-F CP were near the 5-fold axis and were located toward the CP N-terminal half.

In addition to the N-terminal insertion (containing insertion I1), we detected five additional peptide insertion sites on the hPBV outer capsid surface, I2 to I6 (Fig. 5B, upper triangles). The location of insertions toward the CP C-terminal region could constitute a mechanism for acquisition of new functions without compromising CP ability to assemble into a 120-subunit T=1 capsid. The single insertion site on the partitivirus outer capsid surface forms the large arch-like protrusion (including 105 residues) (Fig. 5B, lower triangle).

Asymmetric dimers and pores in the hPBV capsid. A and B subunits in the hPBV Δ45-CP dimer have nearly identical conformations and form symmetric dimers, as

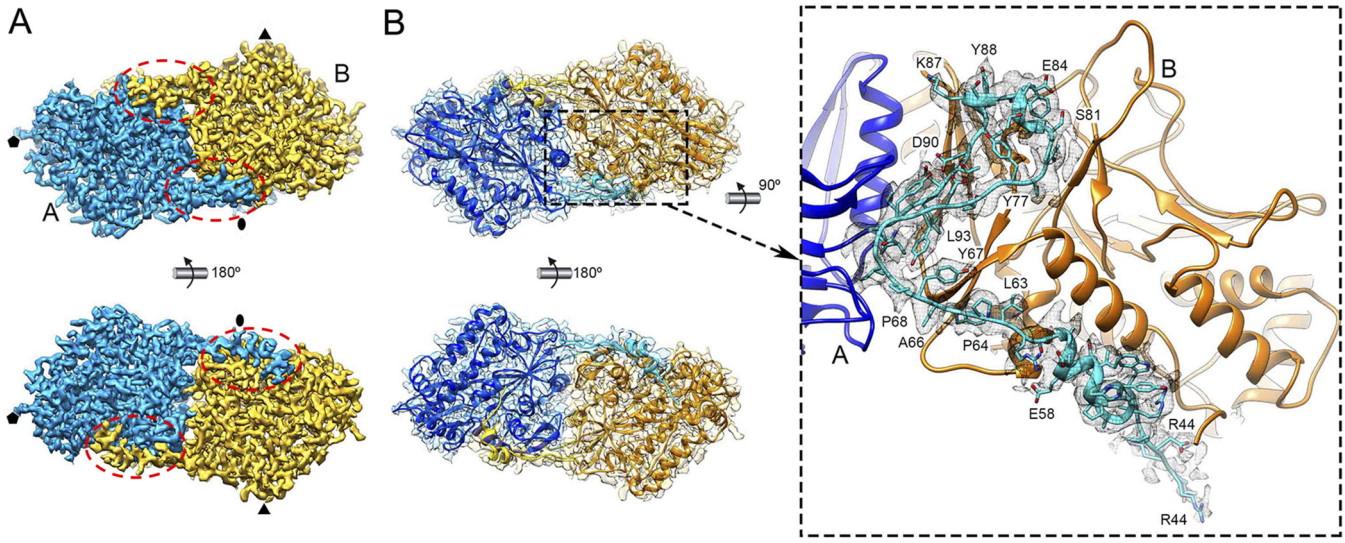

FIG 4 Domain-swapped organization of CP dimers in the hPBV capsid. (A) Cryo-EM density map of the CP dimer (outer surface, top; inner surface, bottom). The A and B subunits are blue and yellow, respectively. Dashed ovals indicate the N-terminal regions swapped between the dimers. (B) Atomic models of the A and B subunits and corresponding density (mesh) (view and color code as in panel A). Swapped regions of A and B subunits are highlighted in light blue and yellow, respectively. The closeup (side view) on the right shows the A-swapped Arg44-Ile95 region (light blue) with its cryo-EM density (gray mesh).

described for the proteolyzed A and B subunits of rPBV. The hPBV nonproteolyzed A and B subunits in the CP dimer have similar conformations (RMSD = 1.8 Å for 506 Cα atoms), but with major differences at the N and C termini that result in asymmetric dimers. Whereas the A subunit N-terminal end (residues Thr43 to Trp49) extends into the capsid interior (Fig. 6A, green), the equivalent B subunit region (Thr43-Val47) interacts with the inner capsid surface (Fig. 6B, green). The disordered CP N terminus has 13 basic residues (of 42), suggesting protein-RNA interactions mediated by A subunits (see below) (Fig. 6C, blue asterisks; Fig. 6D, green circles). The CP-B N terminus, rather than interacting with nucleic acids, might be neutralized by different regions of the highly negative inner dimer surface (Fig. 6D); the situation is similar for hPBV Ht-CP A and B subunits (Fig. 6A and B, pink; Movie S1).

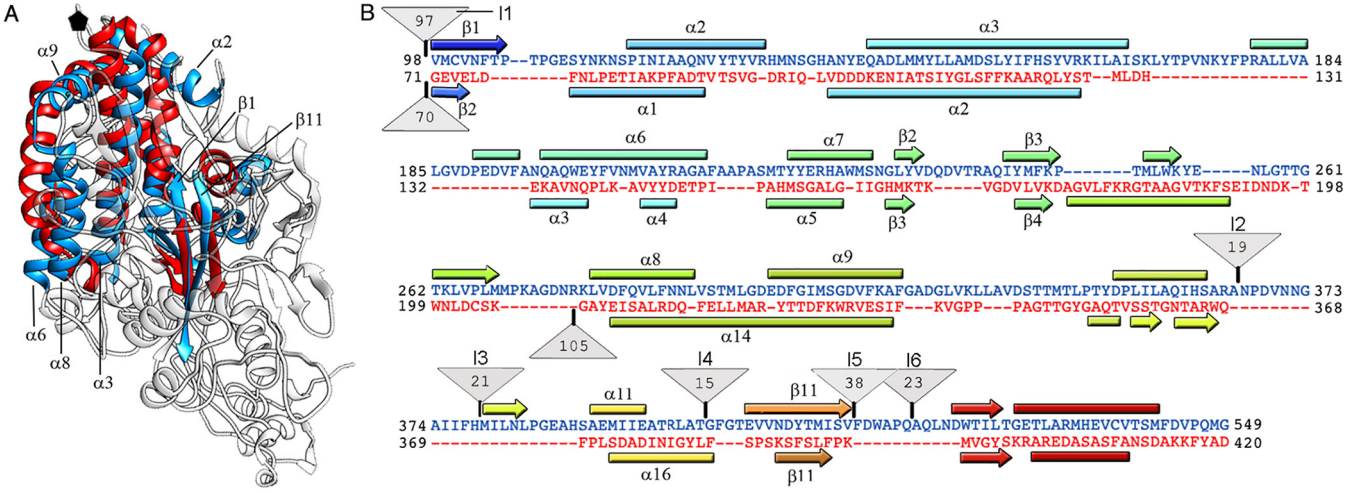

FIG 5 Structural homology of the hPBV and partitivirus capsid proteins. (A) Superimposed hPBV (blue) and PsV-F (red) CP (white regions indicate nonsuperimposed regions for both CP). (B) Sequence alignment of hPBV CP (blue) and PsV-F CP (red) resulting from the Dali structural alignment. The α helices (rectangles) and β strands (arrows) are rainbow-colored from blue (N terminus [N-term]) to red (C terminus [C-term]) for each CP. Triangles represent nonaligned segments or insertions (I1 to I6; sizes [in kilobases] are given in the triangles).

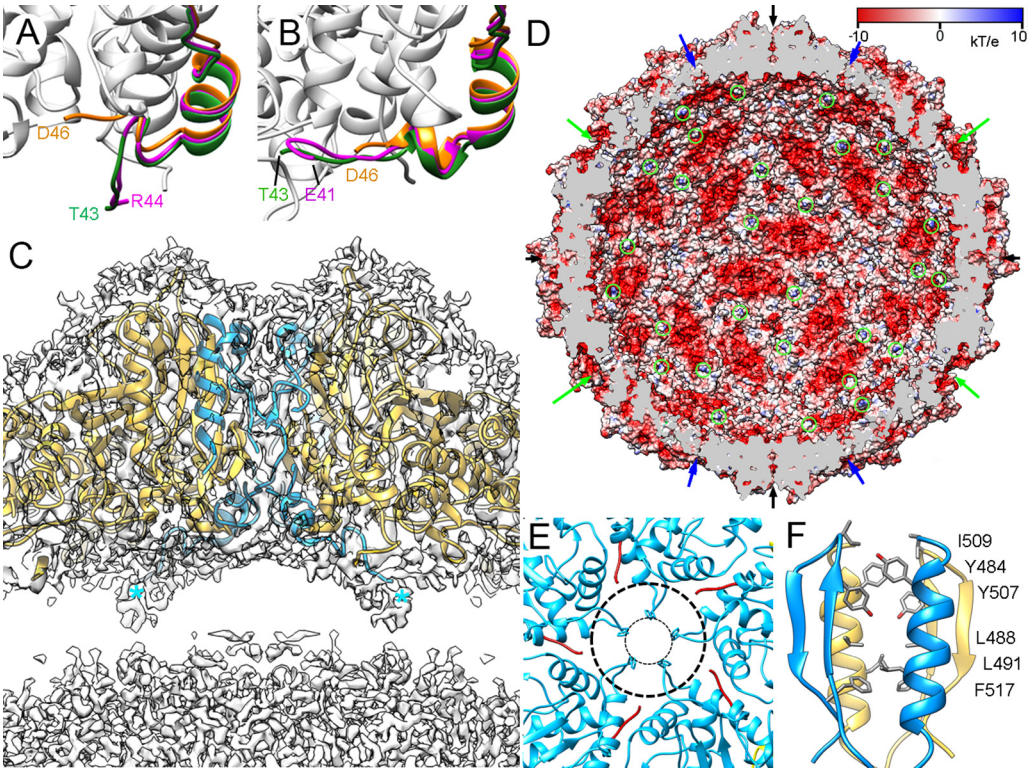

FIG 6 CP N-terminal ends and pore structure in the hPBV capsid. (A and B) Close-up of the visible N-terminal (A) and C-terminal (B) segments of CP (green), Ht-CP (pink), and Δ45-CP (orange). The last visible residue is indicated. (C) Magnified view of a 50-Å-thick slab around an icosahedral 2-fold axis. Atomic model regions of subunits A (blue) and B (yellow) are superimposed on the density map (contoured at 0.5 σ above the mean density). Asterisks indicate N-terminal ends of two A subunits. (D) The hPBV capsid inner surface is represented with electrostatic potentials, showing the distribution of negative (red) and positive (blue) charges. The internal cargo was removed computationally. Arrows indicate capsid pores at the 5-fold (green), 3-fold (blue), and 2-fold (black) axes. The N-terminal ends of A subunits are indicated (green circles). (E) Pores at the 5-fold axes (top view). His135 defines a 9-Å pore opening (inner dashed circle); a rearrangement in the Met131-Tyr138 loop enlarges this pore to 23 Å (outer dashed circle). (F) Numerous polar (top) and hydrophobic (bottom) interactions between local 2-fold-related A and B subunits.

Although the first 42 N-terminal residues of CP are invisible in our atomic model of CP, the electrostatic potential on the capsid inner surface indicated highly negatively charged grooves at the local quasi-2-fold axes (Fig. 6D); these grooves maintain separation of the nucleic acid densities (see below). Most capsid pores are ~5 to 10 Å in diameter (Fig. 6D, arrows); as in other dsRNA viruses, exit of RNA transcripts would thus require conformational changes in CP. Channels at the 5-fold axis are 9 Å in diameter between the His135 side chains in the Met131-Tyr138 loop; a simple conformational change in this loop could result in a 23-Å opening (Fig. 6E). The two α12 helices at the local 2-fold axes enclose a putative channel, doubly occluded by Ile509, Tyr484, and Tyr507 near the outer surface and by a hydrophobic cluster at the bottom region (Phe517, Leu491, and Leu488) (Fig. 6F).

Disassembly/assembly of hPBV virus-like particles. We analyzed the internal content of hPBV CP, Δ45-CP, and Ht-CP VLP by agarose gel electrophoresis and ethidium bromide staining under native conditions. CP and Ht-CP capsids contained nucleic acids, which Δ45-CP lacked (Fig. 7A, right; VLPs lanes 1 [CP], 2 [Ht-CP], and 3 [Δ45-CP]). This was followed by experiments with RNase A or DNase, using as controls the total nucleic acids of HEK293T cells, which contain rRNA and plasmid DNA (Fig. 7A, Control). As the bacterial extract was treated extensively with RNase A, these RNA molecules are associated with intact CP and Ht-CP VLP. Nucleic acids extracted and purified from freshly prepared CP and Ht-CP VLP resolved as two diffuse bands with a large smear (Fig. 7A, NA_{VLP}), which were extensively digested by RNase (Fig. 7A, +RNase) but were DNase resistant (Fig. 7A, +DNase). Next-generation sequencing

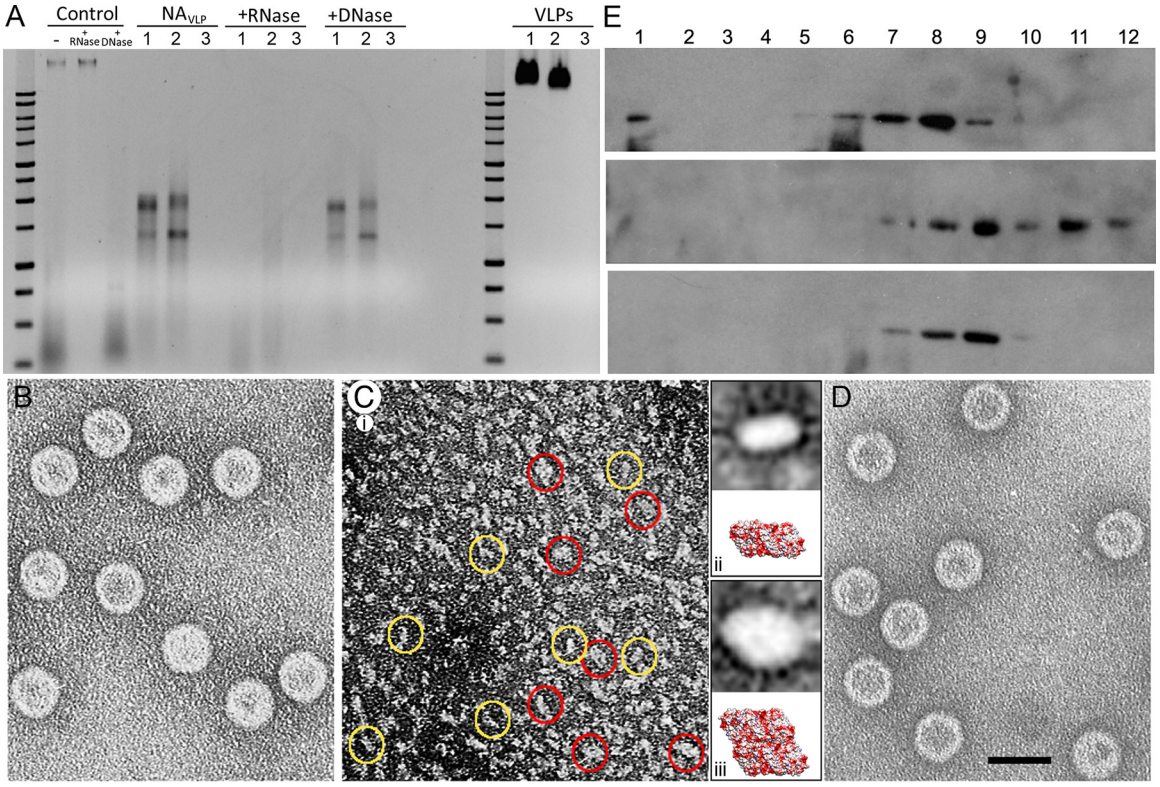

FIG 7 Encapsidated nucleic acids in hPBV are RNase sensitive. Disassembly and reassembly of the T=1 hPBV capsid is reversible. (A) Structurally unaltered hPBV Ht-CP (lanes 1), CP (lanes 2), and Δ45-CP (lanes 3) VLP were analyzed by agarose gel electrophoresis and detected by ethidium bromide staining (VLPs). The same amount of total protein was analyzed for each sample. A 1- kb DNA ladder (10,000 to 250 bp; Promega) was used as a molecular weight marker. Purified nucleic acids from disrupted VLP (NA$_{VLP}$) were treated with RNase (+RNase) or DNase (+DNase). Total nucleic acids of HEK293T cells (Control), which contain rRNA (bottom smear) and plasmid DNA (top band), were used as controls. (B to D) Disassembly/reassembly of the hPBV CP capsid. Electron microscopy and negative staining of purified hPBV CP (B), disassembled capsids (C), and reassembled capsids (D). Two major subassemblies (yellow and red circles) were detected in the disassembled material (C, panel i). Classification and alignment of these subassemblies resulted in average images of ~63 by 112 (C, panel ii, top) and ~105 by 140 Å (C, panel iii, top), with dimensions and morphology similar to those of a CP dimer (C, panel ii, bottom) or tetramer (C, panel iii, bottom). (E) hPBV CP capsids (top), disassembled material (center), and reassembled particles (bottom) were purified by ultracentrifugation on sucrose gradients, collected in 12 fractions, and analyzed by SDS-PAGE and Western blotting using anti-CP antibodies. The sedimentation direction was from right to left, with fraction 12 at the gradient top.

(NGS) analysis showed that ~95% (CP) to ~99% (Ht-CP) of the encapsidated RNA was made up of bacterial rRNA (23S and 16S; the two prominent bands in the agarose gel). A broad representation of bacterial transcripts accounted for the remaining sequences. Mass spectrometry analysis of Δ45-CP capsids showed that they contain diverse host proteins that are probably randomly encapsulated in the crowded cytoplasm (Table S1). Similar analysis showed that in addition to nucleic acids, CP VLP also contained host proteins (Table S2). These results indicate that (i) the basic N-terminal region in CP is responsible for host rRNA encapsidation and (ii) rRNA binding is probably necessary to neutralize repulsive charge interactions between CP (or Ht-CP) but is dispensable for Δ45-CP.

We carried out initial disassembly/reassembly assays with hPBV CP, Δ45-CP, and Ht-CP VLP. After dialysis against buffer A (50 mM Na_2CO_3 [pH 10], 1 M NaCl; 12 h, 20°C), hPBV CP capsids (Fig. 7B) were mostly disassembled, as negative staining electron microscopy detected only small capsomers (Fig. 7C, panel i). We assessed the ability of these components to reassemble by further dialyzing the disassembled material (25 mM Tris HCl [pH 7.5], 50 mM NaCl); the resulting assemblies were isometric particles with size and morphology similar to those of T=1 VLP (Fig. 7D). These particles could not be reassembled if the salt concentration used for disassembly was <1 M. Although the disassembled material is heterogeneous, analysis of this particulate material

indicated at least two basic subassemblies (Fig. 7C, panel i, yellow and red circles). After selecting, classifying, and aligning 516 particles, we obtained two averaged views with an elongated profile (351 particles) (Fig. 7C, panel ii, top) or diamond profile (165 particles) (Fig. 7C, panel iii, top); based on their dimensions, these might, respectively, be CP dimers (Fig. 7C, panel ii, bottom) or tetramers (Fig. 7C, panel iii, bottom). These data suggest that the building units are dimers that can assemble into tetramers (parallel dimers) to form a complete isometric capsid, a triacontahedron (Movie S2).

We processed native, disassembled, and reassembled VLP by ultracentrifugation in linear 20-to-50% sucrose gradients in appropriate buffers and analyzed the resulting fractions by SDS-PAGE and Western blotting using CP-specific antibodies (Fig. 7E). The CP signal for the original native VLP was found in the middle fractions, which contained isometric T=1 capsids. Disassembled VLP migrated to the top of the gradient, and after reassembly in a second dialysis, the CP signal was again detected mostly in the middle fractions. This biochemical analysis confirmed that CP assembly is reversible.

Mechanical properties of hPBV virus-like particles. Although hPBV VLP encapsulate host proteins nonspecifically, CP (and Ht-CP) VLP pack host nucleic acids more efficiently than Δ45-CP VLP due to their basic CP N termini. We used atomic force microscopy (AFM) to analyze the cargo influence on their mechanical properties. Particles attached to freshly cleaved HOPG (highly oriented pyrolytic graphite) substrate were scanned with the tip of the AFM, and those stably attached to the surface were selected. The three particle types showed similar topography and height, indicating minimal VLP deformation after surface adsorption (Fig. 8A). In single indentation experiments on structurally preserved particles, VLP deformations showed linear behavior typical of a shell-like capsid (41) (Fig. 8B). Ht-CP and CP VLP, with spring constants (mean ± standard deviation [SD]) of 0.23 ± 0.08 N/m and 0.27 ± 0.06 N/m, respectively, were softer than Δ45-CP VLP (spring constant, 0.33 ± 0.09 N/m) (Fig. 8C; Δ45-CP, orange; CP, green; Ht-CP, pink). Given the lack of an appropriate tissue culture system, comparison with authentic hPBV virions is not possible. Based on our results, we suggest that the increased rigidity of Δ45-CP VLP is due to the lack of packaged nucleic acids. We hypothesized that the characteristics of CP (and Ht-CP) VLP more closely resemble those of hPBV virions, whose higher flexibility might be necessary for a capsid that replicates and transcribes its genome and remains structurally undisturbed throughout infection.

The ratio between critical deformation ($\delta_{critical}$ [maximum particle deformation before rupture]) and particle height describes critical strain (ε_c), which establishes differences in particle brittleness (42). Ht-CP VLP, with the highest critical strain ($\varepsilon_{c\text{-Ht-CP}} = 0.11 \pm 0.02$), were the least brittle particles (Fig. 8D; Δ45-CP, orange; CP, green; Ht-CP, pink). For CP and Δ45-CP, VLP ε_c was 0.09 ± 0.03 and 0.08 ± 0.02, respectively. Delay in capsid breakage is associated with the presence of heterologous nucleic acids. The results thus indicate that the CP N-terminal segment is involved not only in nucleic acid interaction/packaging but also in modulating the mechanical behavior of the hPBV capsid in conjunction with the packaged cargo.

DISCUSSION

The structure of the hPBV capsid, as well as that of the partitivirus PsV-F (18), suggests that the compact quasisymmetric dimers are the protomers or assembly units. The strongest interaction between hPBV CP dimers occurs at icosahedral 2-fold axes, in which a surface area of 2,644 Å^2 is buried; we consider it likely that assembly proceeds from intermediates as dimers of CP dimers, as suggested for PsV-F (18, 40), and that 30 such diamond-shaped tetramers assemble into a 120-subunit capsid. The presence of CP tetramers in the disassembled hPBV particles is evidence that they could be assembly intermediates. Alternatively, tetramers might be dead-end or kinetically trapped intermediates. We are pursuing the isolation of dimers and/or tetramers by gel filtration chromatography to demonstrate that they assemble into VLP. During capsid

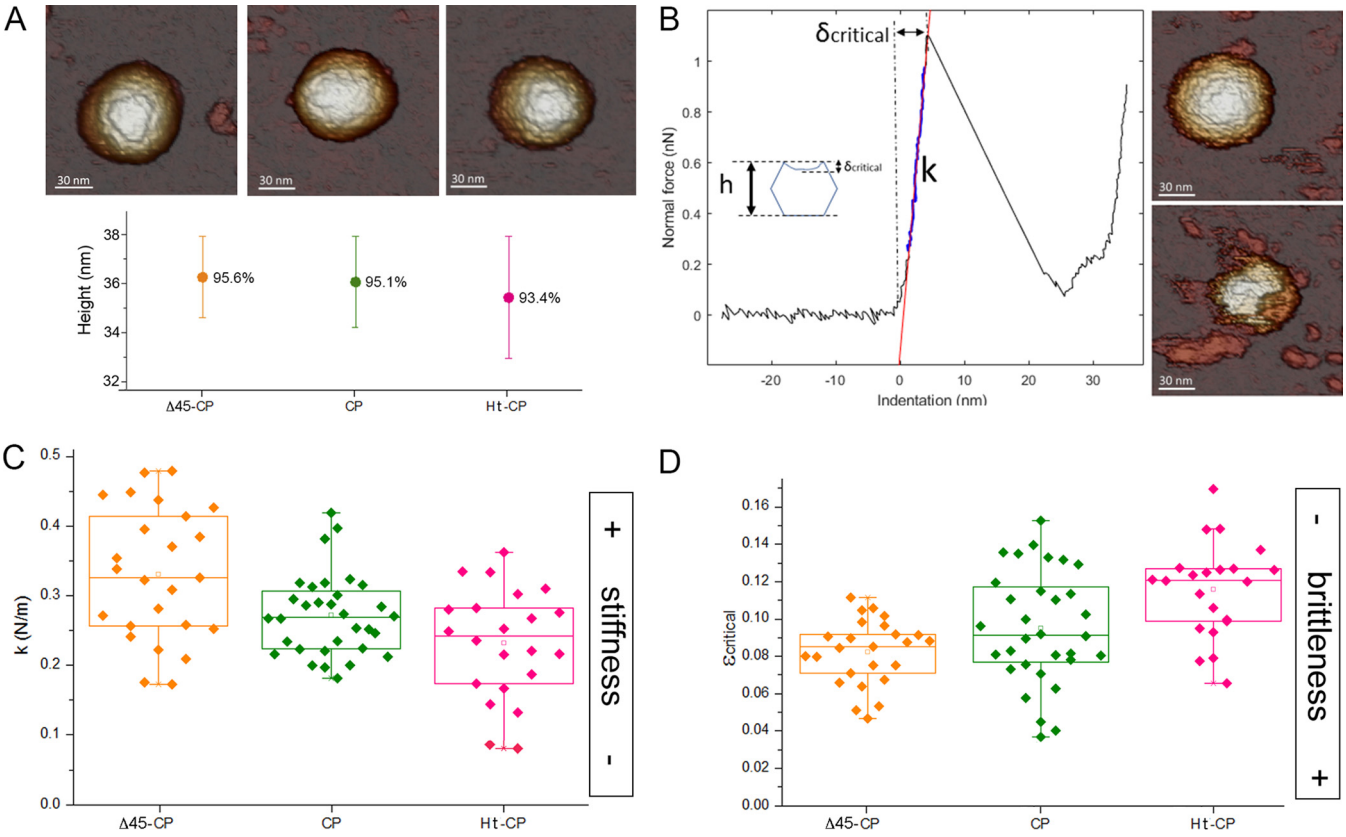

FIG 8 Biophysical properties of hPBV capsids determined by AFM indentations. (A) (Top) AFM topographies of hPBV Δ45-CP (left), CP (center), and Ht-CP (right) particles. (Bottom) Height of hPBV Δ45-CP (orange), CP (green), and Ht-CP (pink) particles after adsorption. Percentages indicate the ratio between average height as measured by AFM and nominal height based on cryo-EM maps. (B) (Left) A force-versus-indentation curve (FIC) of a CP hPBV capsid. Particle stiffness (k) and critical deformation ($\delta_{critical}$) can be calculated from the nanoindentation. (Inset) Critical strain ($\varepsilon_{critical}$), which provides information about particle deformation before breakage, is defined as the ratio between the critical indentation and particle height. (Right) AFM topographies of the hPBV capsid before (top) and after (bottom) breakage. (C and D) Comparison of the average stiffness (C) and fragility (D) of hPBV Δ45-CP (orange), CP (green), and Ht-CP (pink) particles.

assembly of dsRNA phages ϕ6 and ϕ8 (two cystoviruses), the preassembled tetrameric building blocks appear to be obligatory intermediates (43, 44). The assembly pathway of hPBV and rPBV (12) might resemble that of flavivirus (an enveloped [positive-strand] ssRNA virus), which is assembled in a T=3 capsid from 30 diamond tiles made of three parallel dimers of the E glycoprotein (45).

In a baculovirus-based expression system, the rPBV CP N terminus undergoes an intradimer, transproteolytic cleavage, and the released N-terminal segment is post-translationally modified. In addition, a cleavage site mutant CP assembles mostly as unstable and/or broken VLP (12). Using the same strain and *E. coli* as an expression system, our studies and others (38) show that hPBV CP is not processed and assembles as efficiently as hPBV Δ45-CP (and Ht-CP). These data indicate that either an intrinsic CP factor or a host environment-specific component is a major determinant for virus assembly and CP processing. Similar observations were made for other viruses; baculovirus-based expression of the infectious bursal disease virus (IBDV) polyprotein leads to tubular assemblies without CP processing (46, 47); in vaccinia virus-based expression (48), the resulting assemblies are icosahedral particles with a correctly processed CP, like virions.

Despite these drawbacks, the recombinant baculovirus systems provide considerable information. Our 2.6-Å cryo-EM map shows that the N-terminal ends of A and B subunits within the dimer have distinct conformations that lead to asymmetric dimers. Only the N-terminal region of polypeptide chain A (segment Thr43-Trp49), which precedes the invisible basic region, extends and interacts with the heterologous

packaged RNA molecules, probably mimicking its role *in vivo*. Many CP of positive ssRNA viruses (49–51) as well as partitivirus (18) have similar basic N-terminal arms. During hPBV assembly, this interaction would be critical for incorporating the RdRp, which has strong affinity for the conserved 5′-terminal sequence of the viral RNA (38). Our results imply that (i) the basic CP N-terminal region is responsible for host rRNA encapsidation and (ii) rRNA binding is probably necessary to neutralize repulsive charge interactions between CP (or Ht-CP), as in hepatitis B virus (52), plant cowpea chlorotic mottle virus (CCMV) (53), and brome mosaic virus (54). Coassembly of CP and genomic nucleic acids (emulated by host rRNA) is extensive in ssRNA viruses, such as picornaviruses (51), and ssDNA viruses, such as circoviruses (55). This might also apply to dsRNA viruses, which initially nucleate around genomic ssRNA segments (28, 29) that are replicated into dsRNA segments in the capsid interior (reviewed in reference 56).

Whereas the T=1 capsids of reo- and cystoviruses have an average thickness of 15 to 30 Å, this varies in hPBV between 40 and 55 Å, and dsRNA mycovirus capsids are even thicker, ~50 to 75 Å. These features are probably related to additional functions that T=1 capsids have acquired during hPBV and dsRNA mycovirus evolution (57).

In viruses of the family *Reoviridae* and dsRNA phages, the T=1 capsid or innermost core acts as scaffold to prime assembly of the surrounding T=13 capsid (58) (one or two shells), which has a protective role and participates in cell entry (59) (cypoviruses are an exception, with a single capsid layer occluded within a large, proteinaceous polyhedron [60]). Most fungal dsRNA viruses have a single-shell T=1 capsid and lack a strategy for entering host cells. Due to their intimate relationship with their hosts, mycoviruses have nevertheless increased their CP complexity by acquiring new domains, such as the insertions with enzyme activity in L-A virus (61, 62) and in quadrivirus CP (21). Some totivirus-like dsRNA viruses with a single-layer T=1 capsid (like that of L-A virus) can be transmitted extracellularly, such as the protozoan-infecting *Giardia lamblia* virus (GLV) (16) and the shrimp infectious myonecrosis virus (IMNV) (63, 64). IMNV has long fiber complexes at the 5-fold axes that could mediate cell entry. The capsid protein of the metazoan totivirus-like Omono River virus (OmRV) has three surface loops that might have a role in cell entry (65). We hypothesized a dual role for the outer surface insertions in the hPBV single-shell capsid: whereas insertions I1, I5, and I6 stabilize the dimers and thus contribute to capsid stability, insertions I2 to I4 might be involved in receptor binding.

Although there are numerous similarities in capsid structure and assembly between partiti- and picobirnavirus, PBV have an extracellular phase, like *Reoviridae* family viruses and cystoviruses. Reovirus T=1 cores package 9 to 12 RdRp complexes per virion and an equivalent number of dsRNA segments at the same ratio (66, 67). For efficient extracellular transmission, it is likely that PBV is a monoparticulate virus, i.e., both genomic segments are packaged in the same particle. In hPBV, given the size of the two dsRNA genomic segments (4,270 bp), their molar mass is 2.9 MDa (assuming 682 Da/bp). Considering the volume available (12,770 nm^3 based on an average internal capsid radius of 140 Å), the density of two packed dsRNA molecules would be 34 bp/100 nm^3; this resembles the density of multilayered rota- and reoviruses (34 and 38 bp/100 nm^3, respectively), which can reach values of >40 bp/100 nm^3 in cystovirus and bluetongue virus (for a review, see reference 57). This tight packing contrasts with the loosely packed dsRNA in fungal viruses (including partitivirus), with a genome density of ~20 bp/100 nm^3, as they pack a single dsRNA molecule per capsid, although most have multisegmented genomes (68).

The AFM studies show that CP and Ht-CP are softer and less brittle than Δ45-CP VLP. The Δ45-CP capsid, which practically lacks nucleic acids, has a negatively charged inner surface, common to many dsRNA virus capsids. The CP (and Ht-CP) capsid is decorated with the basic N-terminal segments that are structurally disordered (or invisible), and only tiny connections with the internal nucleic acids can be seen in A subunits. Although all these VLP are far from being authentic virions, those containing host

nucleic acids might represent a configuration closer to that of native virions. More important, the basic segments remain within the capsids, covalently bound to the inner capsid surface, as in the case of hPBV CP, or unbound, as in rPBV Δ65-CP. In both situations, this N-terminal segment is likely to interact electrostatically with the nucleic acids. Whereas intense electrostatic repulsion would increase stiffness, charge neutralization would lead to slightly softer VLP, with delayed capsid breakage. Δ45-CP VLP rigidity could be due to the heterologous cargo proteins and/or the D46-A48 N-terminal segment, which is parallel to the inner shell surface and would act as a molecular staple. Although this appears to be only a tiny structural difference, mechanical stiffening of a virus capsid can be modified with single mutations (69, 70).

Our AFM results suggest that nucleic acid-containing hPBV capsids become flexible and/or acquire dynamic status. This contrasts with previous AFM studies in which, for example, the high internal pressure of phage ϕ29-packaged dsDNA increases particle rigidity (71). The 60-dimer T=1 capsid is a transcriptional or replicative active particle in the host cytoplasm; for these processes, the capsid must be a dynamic platform that increases pore size and facilitates template motion in its interior. In the multilayered BTV, removal of outer capsid proteins changes the curvature of the inner core, inducing outward movement of inner capsid proteins around the 5-fold axis (2). Further studies are needed to verify the hypothesis that the viral genome (such as ssRNA or dsRNA) provides dynamism to the 60-dimer T=1 capsid. It will be crucial to compare biophysical properties of empty and dsRNA-containing hPBV virions in a quiescent state with those of virions synthesizing actively RNA molecules. We are currently evaluating the purification of authentic PBV virions using a reverse-genetics system. Reo- and mycoviruses are also excellent candidates to extend these analyses.

MATERIALS AND METHODS

Construction of recombinant plasmids for bacterial expression. The complete sequences of hPBV segment 1 and 2 strain Hy005102 (GenBank accession number NC_007026 [37]) were ordered from GenScript, produced synthetically, and cloned into plasmid pUC57. HT-CP, CP, and Δ45-CP coding sequences were amplified by PCR from the plasmid with segment 1 using the forward primers 5′-GCGCGGATCCATGAAACAGAATGATACTAAGAAAAC, 5′-GCGCCATATGAAACAGAATGATACTAAGAAAAC, and 5′-GCGCCATATGGACGTTGCTTGGTATGCTCG, respectively, and 3′-GCGCAAGCTTTTATTTGTTGAAGCCCATCTGAG GAAC as the reverse primer for all. The resulting DNA fragments were digested with NdeI and HindIII (CP and Δ45-CP) or with BamHI and HindI II (Ht-CP) and ligated into plasmid pRSETA (Invitrogen), which had previously been digested with appropriate enzymes. NdeI restriction sites allowed removal of the histidine tag from the pRSETA multiple-cloning site in CP and Δ45-CP constructs. Competent *E. coli* DH5α cells were transformed with the ligated products. Ampicillin-resistant clones for each CP variant were selected and sequenced. Positive recombinant plasmids were transformed into the *E. coli* BL21(DE3)pLysS expression strain (Invitrogen). Several ampicillin- and chloramphenicol-resistant clones for each CP variant were examined in a small-scale expression test, and the best clone for each was selected for preparative scale expression.

Expression and purification of hPBV capsids. Bacteria from isolated colonies of previously selected clones were grown (16 h, 37°C) in LB medium with ampicillin (100 μg/ml) and chloramphenicol (35 μg/ml). This preinoculum was diluted 1:10 in prewarmed LB containing the same antibiotics and cultured (37°C) to an A_{600} of 0.17 to 0.2. The culture was equilibrated to 16°C (20 to 30 min), and recombinant protein expression was induced with 1 mM IPTG (isopropyl-β-D-thiogalactopyranoside; 16 h, 16°C). Cells were then chilled on ice, harvested by centrifugation (5,000 $\times$ *g*, 10 min, 4°C), and stored at −20°C until purification.

For hPBV VLP purification, cells were thawed and lysed (1 h, 37°C) in TN buffer (25 mM Tris-HCl [pH 7.5], 50 mM NaCl) containing 50 mM $MgCl_2$, 2% Triton X-100, 0.01 mg/ml RNase A, 0.005 mg/ml DNase I, 0.05 mM dithiothreitol (DTT), 0.25 mg/ml lysozyme, and 1 mM phenylmethylsulfonyl fluoride (PMSF). The lysate was cleared of cell debris by centrifugation (5,000 $\times$ *g*, 10 min, 4°C), and the supernatant was loaded on a 20% sucrose cushion and centrifuged (170,000 $\times$ *g*, 130 min, 4°C). The resulting pellet was resuspended in TN buffer, cleared of insoluble material by centrifugation (20,000 $\times$ *g*, 1 min, 20°C), loaded on a linear 20-to-50% sucrose gradient, and centrifuged (200,000 $\times$ *g*, 45 min, 4°C). The gradient was fractioned into 12 aliquots, which were concentrated by centrifugation (240,000 $\times$ *g*, 2 h, 4°C); pellets were resuspended in TN buffer and stored at 4°C.

Protein identification by mass spectrometry analysis. Purified CP and Δ45-CP VLP were loaded on an SDS-PAGE gel (4% stacking, 12% resolving). Separation was terminated as soon as the front entered 1 cm into the resolving gel, so that the whole proteome was concentrated at the stacking/resolving gel interface. Unseparated protein bands were visualized by Coomassie staining, excised, and digested with trypsin (4 h, 37°C) as described previously (72). Resulting peptides were analyzed by one-dimensional (1D) nanoscale liquid chromatography electrospray ionization-tandem mass spectrometry (nano-LC ESI-MS/MS) using a nano-liquid chromatography system (Eksigent Technol-

ogies nanoLC Ultra 1D plus; SCIEX, Foster City, CA) coupled to a high-speed TripleTOF 5600 mass spectrometer (SCIEX) (73).

Purification of total RNA from hPBV CP and Ht-CP VLP. To isolate the encapsidated RNA, purified CP and Ht-CP VLP in TN buffer were adjusted to 1% SDS, and the proteins were denatured by heating (3 min, 98°C) followed by incubation on ice. Proteinase K was added to a 2-mg/ml final concentration, and samples were incubated with gentle agitation (2 h, 37°C). After protease digestion, RNA was isolated using TRIzol reagent following the manufacturer's instructions (Invitrogen, Carlsbad, CA), further purified using the QIAquick PCR purification kit (Qiagen, Venlo, The Netherlands) according to the manufacturer's protocols, eluted in diethyl pyrocarbonate (DEPC)-treated water, aliquoted, and stored at −80°C.

RNA-Seq. Total RNA (50 ng) from purified CP or Ht-CP VLP was used to construct stranded libraries using the ScriptSeq v2 RNA-Seq library preparation kit following the manufacturer's instructions (Illumina, San Diego, CA). Sample and library quality were determined using a 2100 Bioanalyzer (Agilent). We obtained 75-bp paired-end reads using an Illumina NextSeq 500 benchtop sequencer. Quality was controlled using Fast QC version 0.11.5 (Babraham Institute, Babraham, Cambridgeshire, UK).

Relative transcript abundance was calculated from transcriptome sequencing (RNA-Seq) data using Rockhopper v2.0.3 (74, 75) and *E. coli* BL21-Gold(DE3)pLysS AG genome annotation (NCBI RefSeq no. NC_012947.1). For validation, the same analysis was performed using EDGE-pro (76), with good agreement between the results of the two pipelines.

Atomic force microscopy. For AFM measurements, fresh Δ45-CP, CP, or Ht-CP VLP samples were used. A drop of sample (~30 μl at 0.25 mg/ml in TN buffer) was incubated on a freshly cleaved HOPG piece (ZYA quality; NT-MDT). The AFM (Nanotec Electrónica SL, Madrid, Spain) was operated in Jumping Mode Plus in liquid (77) using rectangular cantilevers (RC800PSA; Olympus, Tokyo, Japan) with nominal spring constants of 0.05 N m^{-1}. Cantilever spring constants were routinely calibrated by the Sader method (78). To determine VLP mechanical properties, individual indentation experiments (force versus z-piezo displacement [FZ]) (41) were carried out on single particles. hPBV particles were located by scanning 1-μm areas, and a single particle was focused on by zooming up to a 150-nm area scan. The lateral piezo scan was stopped when the tip was on top of the particle, and force indentation was applied to it. A subsequent image revealed any structural change. The maximum force applied during each indentation was sufficient to induce virus disruption. The FZ speed was approximately 50 nm/s. Images were processed using WSxM software (79).

Cryo-EM and data collection. Purified hPBV samples (5 μl) were applied onto R2/2 300 mesh copper grids (Quantifoil Micro Tools, Jena, Germany) and vitrified using a Leica EM CPC cryofixation unit. Data were collected on an FEI Titan Krios electron microscope operated at 300 kV, and images were recorded on a FEI Falcon III detector operating in linear mode. A total of 2,811 (Ht-CP), 2,360 (CP), and 1,990 (Δ45-CP) movies were recorded at a calibrated magnification of ×75,000, yielding a pixel size of 1.065 Å on the specimen. Each movie comprises 45 frames at an exposure rate of 1.56 e^- $Å^{-2}$ per frame, with 15 s total exposure time and an accumulated dose of 70.2 e^- $Å^{-2}$. Data were acquired with EPU automated data acquisition software for single-particle analysis (Thermo Fisher) with four shots per hole at −0.8 μm to −3.5 μm defocus.

Image processing. Movies were motion corrected and dose weighted with Motioncor2 (80). Aligned, non-dose-weighted micrographs were then used to estimate the contrast transfer function (CTF) with CTFfind4 (81). All subsequent image processing steps were performed using RELION 2.1 (82) within Scipion (83). 2D averages from preliminary data sets were used as references to automatically pick the micrographs, and a total of 129,227 (Ht-CP), 135,314 (CP), and 103,959 (Δ45-CP) particles were extracted. The three data sets used for 2D classification were applied for a 3D classification imposing icosahedral symmetry, with an initial model from preliminary data sets low-pass filtered to 40-Å resolution. The best 30,342 (Ht-CP), 102,722 (CP), and 51,194 (Δ45-CP) particles were included in 3D autorefinement, again imposing icosahedral symmetry, yielding maps with an overall resolution at 2.80 Å (Ht-CP), 2.63 Å (CP), and 2.80 Å (Δ45-CP) based on the gold standard (FSC = 0.143) criterion. Local resolution was estimated using Monores (84).

Model building and refinement. The crystal structure of rabbit PBV (PDB 2VF1) (12) was used as a template to build a homology model with the hPBV sequence using the Swiss-Model server (https://swissmodel.expasy.org). The output model was first manually docked as a rigid body into the density, followed by real space fitting with the Fit in Map routine in UCSF Chimera (85). The model was then manually rebuilt in Coot (86) to optimize fit to density; Phenix (87) was used for real space refinement. Refinement statistics are listed in Table 1.

Model validation and analysis. The FSC curve between the final model and the map after postprocessing in RELION (Model versus Map) is shown in Fig. 2B. For cross-validation against overfitting, the atoms in the final atomic model were displaced by 0.5 Å in random directions using Phenix. The shifted coordinates were then refined against one of the half-maps (work set) in Phenix, using the same procedure as for refinement of the final model. The other half-map (test set) was not used in refinement for cross-validation. FSC curves of the refined shifted model against the work set (FSCwork) and against the test set (FSCtest)were calculated. The FSCwork and FSCtest curves are not significantly different, consistent with absence of overfitting in the final models (data not shown; available upon request). The atomic model quality was assessed and validated with Coot, with MolProbity (88) as implemented in Phenix, and with the Worldwide PDB (wwPDB) OneDep System (https://deposit-pdbe.wwpdb.org/deposition). Graphics were produced by UCSF Chimera (89).

Data availability. The atomic coordinates have been deposited in the Protein Data Bank with codes 6Z8D, 6Z8E, and 6Z8F for hPBV CP, htCP, and Δ45-CP, respectively. The cryo-EM density maps are

TABLE 1 Cryo-EM data collection and refinement statistics for hPBV Ht-CP, CP, and Δ45-CP capsids

Parameter	Ht-CP (EMD-11116, PDB 6Z8E)	CP (EMD-11115, PDB 6Z8D)	Δ45-CP (EMD-11117, PDB 6Z8F)
Data collection and processing			
Microscope	FEI Titan Krios	FEI Titan Krios	FEI Titan Krios
Detector	Falcon III (linear mode)	Falcon III (linear mode)	Falcon III (linear mode)
Magnification	×75,000	×75,000	×75,000
Voltage (kV)	300	300	300
Electron exposure (e^{-}/Å^2)	70.2	70.2	70.2
Exposure per frame (e^{-}/Å^2)	1.56	1.56	1.56
Defocus range (μm)	−0.50 to −4.0	−0.50 to −4.0	−0.50 to −4.0
Pixel size (Å)	1.065	1.065	1.065
Micrographs collected (no.)	2,811	2,360	1,990
Initial particles (no.)	129,227	135,314	103,959
Final particles (no.)	30,342	102,722	51,194
Symmetry imposed	I2	I2	I2
Map resolution (Å)	2.80	2.63	2.80
FSC threshold	0.143	0.143	0.143
Map resolution range (Å)	2.69–3.50	2.51–3.05	2.56–3.80
Refinement			
Model resolution (Å)	2.84	2.65	2.83
FSC threshold	0.5	0.5	0.5
Mask correlation coefficient	0.87	0.84	0.87
Map sharpening B factor (Å^2)	−146	−152	−159
Model composition (asymmetric subunit)			
Nonhydrogen atoms	8,046	8,038	7,986
Protein residues	1,018	1,017	1,011
ADP (B factors), min/max/mean	6.53/46.51/16.01	2.89/62.45/10.32	4.66/42.52/12.70
RMSD			
Bond lengths (Å)	0.006	0.005	0.007
Bond angles (°)	0.794	0.823	0.861
Validation			
MolProbity score	1.52	1.51	1.58
Clashscore	3.60	4.23	4.45
Rotamer outliers (%)	0.23	0.35	0.12
Ramachandran plot			
Favored (%)	94.67	95.56	94.84
Allowed (%)	5.33	4.34	4.97
Outliers (%)	0.00	0.10	0.20

deposited in the EM Data Bank with codes EMD-11115, EMD-11116, and EMD-11117 for hPBV CP, Ht-CP, and Δ45-CP, respectively.

SUPPLEMENTAL MATERIAL

Supplemental material is available online only.

SUPPLEMENTAL FILE 1, MOV file, 5.3 MB.

SUPPLEMENTAL FILE 2, MOV file, 16.8 MB.

SUPPLEMENTAL FILE 3, XLSX file, 0.2 MB.

SUPPLEMENTAL FILE 4, XLSX file, 0.1 MB.

SUPPLEMENTAL FILE 5, PDF file, 0.02 MB.

ACKNOWLEDGMENTS

We thank Amelia Nieto and Alejandra Pazo for providing total nucleic acids of HEK293T cells, José L. Carrascosa (CSIC) for critical readings of the manuscript, and C. Mark for editorial assistance. We thank the personnel of the Cryo-EM Facility of the Centro Nacional de Biotecnología-Centro de Investigaciones Biológicas (CNB-CIB) in Madrid, Spain, and of the Astbury BioStructure Laboratory at the University of Leeds for their help during cryo-EM data acquisition. The proteomic analyses were performed in the CNB-CSIC Proteomics Facility, part of ProteoRed, PRB3-ISCIII, supported by grant PT17/0019.

This work was supported by grants from the Spanish Ministry of Economy and Competitivity (BFU2017-88736-R) and the Comunidad Autónoma de Madrid (P2018/NMT-4389) to J.R.C.

REFERENCES

1. Patton JT. 2008. Segmented double-stranded RNA viruses. Structure and molecular biology. Caister Academic Press, Norfolk, United Kingdom.
2. He Y, Shivakoti S, Ding K, Cui Y, Roy P, Zhou ZH. 2019. In situ structures of RNA-dependent RNA polymerase inside bluetongue virus before and after uncoating. Proc Natl Acad Sci U S A 116:16535–16540. https://doi.org/10.1073/pnas.1905849116.
3. Ding K, Celma CC, Zhang X, Chang T, Shen W, Atanasov I, Roy P, Zhou ZH. 2019. In situ structures of rotavirus polymerase in action and mechanism of mRNA transcription and release. Nat Commun 10:2216. https://doi.org/10.1038/s41467-019-10236-7.
4. Cui Y, Zhang Y, Zhou K, Sun J, Zhou ZH. 2019. Conservative transcription in three steps visualized in a double-stranded RNA virus. Nat Struct Mol Biol 26:1023–1034. https://doi.org/10.1038/s41594-019-0320-0.
5. Lahiri I, Xu J, Han BG, Oh J, Wang D, DiMaio F, Leschziner AE. 2019. 3.1A structure of yeast RNA polymerase II elongation complex stalled at a cyclobutane pyrimidine dimer lesion solved using streptavidin affinity grids. J Struct Biol 207:270–278. https://doi.org/10.1016/j.jsb.2019.06.004.
6. Arnold MM, Sen A, Greenberg HB, Patton JT. 2013. The battle between rotavirus and its host for control of the interferon signaling pathway. PLoS Pathog 9:e1003064. https://doi.org/10.1371/journal.ppat.1003064.
7. Nuss DL. 2011. Mycoviruses, RNA silencing, and viral RNA recombination. Adv Virus Res 80:25–48. https://doi.org/10.1016/B978-0-12-385987-7.00002-6.
8. Settembre EC, Chen JZ, Dormitzer PR, Grigorieff N, Harrison SC. 2011. Atomic model of an infectious rotavirus particle. EMBO J 30:408–416. https://doi.org/10.1038/emboj.2010.322.
9. Grimes JM, Burroughs JN, Gouet P, Diprose JM, Malby R, Zientara S, Mertens PP, Stuart DI. 1998. The atomic structure of the Bluetongue virus core. Nature 395:470–478. https://doi.org/10.1038/26694.
10. Reinisch KM, Nibert ML, Harrison SC. 2000. Structure of the reovirus core at 3.6 Å resolution. Nature 404:960–967. https://doi.org/10.1038/35010041.
11. Yu X, Jin L, Zhou ZH. 2008. 3.88 A structure of cytoplasmic polyhedrosis virus by cryo-electron microscopy. Nature 453:415–419. https://doi.org/10.1038/nature06893.
12. Duquerroy S, Da Costa B, Henry C, Vigouroux A, Libersou S, Lepault J, Navaza J, Delmas B, Rey FA. 2009. The picobirnavirus crystal structure provides functional insights into virion assembly and cell entry. EMBO J 28:1655–1665. https://doi.org/10.1038/emboj.2009.109.
13. Nemecek D, Boura E, Wu W, Cheng N, Plevka P, Qiao J, Mindich L, Heymann JB, Hurley JH, Steven AC. 2013. Subunit folds and maturation pathway of a dsRNA virus capsid. Structure 21:1374–1383. https://doi.org/10.1016/j.str.2013.06.007.
14. El Omari K, Sutton G, Ravantti JJ, Zhang H, Walter TS, Grimes JM, Bamford DH, Stuart DI, Mancini EJ. 2013. Plate tectonics of virus shell assembly and reorganization in phage phi8, a distant relative of mammalian reoviruses. Structure 21:1384–1395. https://doi.org/10.1016/j.str.2013.06.017.
15. Naitow H, Tang J, Canady M, Wickner RB, Johnson JE. 2002. L-A virus at 3.4 A resolution reveals particle architecture and mRNA decapping mechanism. Nat Struct Biol 9:725–728. https://doi.org/10.1038/nsb844.
16. Janssen ME, Takagi Y, Parent KN, Cardone G, Nibert ML, Baker TS. 2015. Three-dimensional structure of a protozoal double-stranded RNA virus that infects the enteric pathogen Giardia lamblia. J Virol 89:1182–1194. https://doi.org/10.1128/JVI.02745-14.
17. Parent KN, Takagi Y, Cardone G, Olson NH, Ericsson M, Yang M, Lee Y, Asara JM, Fichorova RN, Baker TS, Nibert ML. 2013. Structure of a protozoan virus from the human genitourinary parasite Trichomonas vaginalis. mBio 4:e00056-13. https://doi.org/10.1128/mBio.00056-13.
18. Pan J, Dong L, Lin L, Ochoa WF, Sinkovits RS, Havens WM, Nibert ML, Baker TS, Ghabrial SA, Tao YJ. 2009. Atomic structure reveals the unique capsid organization of a dsRNA virus. Proc Natl Acad Sci U S A 106:4225–4230. https://doi.org/10.1073/pnas.0812071106.
19. Tang J, Ochoa WF, Li H, Havens WM, Nibert ML, Ghabrial SA, Baker TS. 2010. Structure of Fusarium poae virus 1 shows conserved and variable elements of partitivirus capsids and evolutionary relationships to picobirnavirus. J Struct Biol 172:363–371. https://doi.org/10.1016/j.jsb.2010.06.022.
20. Miyazaki N, Salaipeth L, Kanematsu S, Iwasaki K, Suzuki N. 2015. Megabirnavirus structure reveals a putative 120-subunit capsid formed by asymmetrical dimers with distinctive large protrusions. J Gen Virol 96:2435–2441. https://doi.org/10.1099/vir.0.000182.
21. Mata CP, Luque D, Gómez-Blanco J, Rodríguez JM, González JM, Suzuki N, Ghabrial SA, Carrascosa JL, Trus BL, Castón JR. 2017. Acquisition of functions on the outer capsid surface during evolution of double-stranded RNA fungal viruses. PLoS Pathog 13:e1006755. https://doi.org/10.1371/journal.ppat.1006755.
22. Luque D, Gómez-Blanco J, Garriga D, Brilot AF, González JM, Havens WM, Carrascosa JL, Trus BL, Verdaguer N, Ghabrial SA, Castón JR. 2014. Cryo-EM near-atomic structure of a dsRNA fungal virus shows ancient structural motifs preserved in the dsRNA viral lineage. Proc Natl Acad Sci U S A 111:7641–7646. https://doi.org/10.1073/pnas.1404330111.
23. Castón JR, Luque D, Gómez-Blanco J, Ghabrial SA. 2013. Chrysovirus structure: repeated helical core as evidence of gene duplication. Adv Virus Res 86:87–108. https://doi.org/10.1016/B978-0-12-394315-6.00004-0.
24. Coulibaly F, Chevalier C, Gutsche I, Pous J, Navaza J, Bressanelli S, Delmas B, Rey FA. 2005. The birnavirus crystal structure reveals structural relationships among icosahedral viruses. Cell 120:761–772. https://doi.org/10.1016/j.cell.2005.01.009.
25. Saugar I, Luque D, Ona A, Rodríguez JF, Carrascosa JL, Trus BL, Castón JR. 2005. Structural polymorphism of the major capsid protein of a double-stranded RNA virus: an amphipathic alpha helix as a molecular switch. Structure 13:1007–1017. https://doi.org/10.1016/j.str.2005.04.012.
26. Abrescia NG, Bamford DH, Grimes JM, Stuart DI. 2012. Structure unifies the viral universe. Annu Rev Biochem 81:795–822. https://doi.org/10.1146/annurev-biochem-060910-095130.
27. Bamford DH, Grimes JM, Stuart DI. 2005. What does structure tell us about virus evolution? Curr Opin Struct Biol 15:655–663. https://doi.org/10.1016/j.sbi.2005.10.012.
28. Sung PY, Roy P. 2014. Sequential packaging of RNA genomic segments during the assembly of Bluetongue virus. Nucleic Acids Res 42:13824–13838. https://doi.org/10.1093/nar/gku1171.
29. Lourenco S, Roy P. 2011. In vitro reconstitution of Bluetongue virus infectious cores. Proc Natl Acad Sci U S A 108:13746–13751. https://doi.org/10.1073/pnas.1108667108.
30. Borodavka A, Desselberger U, Patton JT. 2018. Genome packaging in multi-segmented dsRNA viruses: distinct mechanisms with similar outcomes. Curr Opin Virol 33:106–112. https://doi.org/10.1016/j.coviro.2018.08.001.
31. Delmas B, Attoui H, Ghosh S, Malik YS, Mundt E, Vakharia VN, Ictv RC. 2019. ICTV virus taxonomy profile: Picobirnaviridae. J Gen Virol 100:133–134. https://doi.org/10.1099/jgv.0.001186.
32. Pereira HG, Flewett TH, Candeias JA, Barth OM. 1988. A virus with a bisegmented double-stranded RNA genome in rat (Oryzomys nigripes) intestines. J Gen Virol 69:2749–2754. https://doi.org/10.1099/0022-1317-69-11-2749.
33. Shi M, Lin XD, Tian JH, Chen LJ, Chen X, Li CX, Qin XC, Li J, Cao JP, Eden JS, Buchmann J, Wang W, Xu J, Holmes EC, Zhang YZ. 2016. Redefining the invertebrate RNA virosphere. Nature 540:539–543. https://doi.org/10.1038/nature20167.
34. Boros A, Polgar B, Pankovics P, Fenyvesi H, Engelmann P, Phan TG, Delwart E, Reuter G. 2018. Multiple divergent picobirnaviruses with functional prokaryotic Shine-Dalgarno ribosome binding sites present in cloacal sample of a diarrheic chicken. Virology 525:62–72. https://doi.org/10.1016/j.virol.2018.09.008.
35. Wolf YI, Kazlauskas D, Iranzo J, Lucia-Sanz A, Kuhn JH, Krupovic M, Dolja VV, Koonin EV. 2018. Origins and evolution of the global RNA virome. mBio 9:e02329-18. https://doi.org/10.1128/mBio.02329-18.
36. Smits SL, van Leeuwen M, Schapendonk CM, Schurch AC, Bodewes R, Haagmans BL, Osterhaus AD. 2012. Picobirnaviruses in the human respiratory tract. Emerg Infect Dis 18:1539–1540. https://doi.org/10.3201/eid1809.120507.
37. Wakuda M, Pongsuwanna Y, Taniguchi K. 2005. Complete nucleotide sequences of two RNA segments of human picobirnavirus. J Virol Methods 126:165–169. https://doi.org/10.1016/j.jviromet.2005.02.010.
38. Collier AM, Lyytinen OL, Guo YR, Toh Y, Poranen MM, Tao YJ. 2016. Initiation of RNA polymerization and polymerase encapsidation by a small dsRNA virus. PLoS Pathog 12:e1005523. https://doi.org/10.1371/journal.ppat.1005523.

39. Holm L, Rosenstrom P. 2010. Dali server: conservation mapping in 3D. Nucleic Acids Res 38:W545–W549. https://doi.org/10.1093/nar/gkq366.
40. Nibert ML, Tang J, Xie J, Collier AM, Ghabrial SA, Baker TS, Tao YJ. 2013. 3D structures of fungal partitiviruses. Adv Virus Res 86:59–85. https://doi.org/10.1016/B978-0-12-394315-6.00003-9.
41. Ivanovska IL, de Pablo PJ, Ibarra B, Sgalari G, MacKintosh FC, Carrascosa JL, Schmidt CF, Wuite GJ. 2004. Bacteriophage capsids: tough nanoshells with complex elastic properties. Proc Natl Acad Sci U S A 101:7600–7605. https://doi.org/10.1073/pnas.0308198101.
42. Llauro A, Luque D, Edwards E, Trus BL, Avera J, Reguera D, Douglas T, Pablo PJ, Castón JR. 2016. Cargo-shell and cargo-cargo couplings govern the mechanics of artificially loaded virus-derived cages. Nanoscale 8:9328–9336. https://doi.org/10.1039/c6nr01007e.
43. Poranen MM, Tuma R, Bamford DH. 2005. Assembly of double-stranded RNA bacteriophages. Adv Virus Res 64:15–43. https://doi.org/10.1016/S0065-3527(05)64002-X.
44. Kainov DE, Butcher SJ, Bamford DH, Tuma R. 2003. Conserved intermediates on the assembly pathway of double-stranded RNA bacteriophages. J Mol Biol 328:791–804. https://doi.org/10.1016/s0022-2836(03)00322-x.
45. Kuhn RJ, Zhang W, Rossmann MG, Pletnev SV, Corver J, Lenches E, Jones CT, Mukhopadhyay S, Chipman PR, Strauss EG, Baker TS, Strauss JH. 2002. Structure of dengue virus: implications for flavivirus organization, maturation, and fusion. Cell 108:717–725. https://doi.org/10.1016/s0092-8674(02)00660-8.
46. Chevalier C, Lepault J, Erk I, Da Costa B, Delmas B. 2002. The maturation process of pVP2 requires assembly of infectious bursal disease virus capsids. J Virol 76:2384–2392. https://doi.org/10.1128/jvi.76.5.2384-2392.2002.
47. Irigoyen N, Castón JR, Rodríguez JF. 2012. Host proteolytic activity is necessary for infectious bursal disease virus capsid protein assembly. J Biol Chem 287:24473–24482. https://doi.org/10.1074/jbc.M112.356113.
48. Lombardo E, Maraver A, Castón JR, Rivera J, Fernández-Arias A, Serrano A, Carrascosa JL, Rodríguez JF. 1999. VP1, the putative RNA-dependent RNA polymerase of infectious bursal disease virus, forms complexes with the capsid protein VP3, leading to efficient encapsidation into virus-like particles. J Virol 73:6973–6983. https://doi.org/10.1128/JVI.73.8.6973-6983.1999.
49. Patel N, Wroblewski E, Leonov G, Phillips SEV, Tuma R, Twarock R, Stockley PG. 2017. Rewriting nature's assembly manual for a ssRNA virus. Proc Natl Acad Sci U S A 114:12255–12260. https://doi.org/10.1073/pnas.1706951114.
50. Borodavka A, Tuma R, Stockley PG. 2012. Evidence that viral RNAs have evolved for efficient, two-stage packaging. Proc Natl Acad Sci U S A 109:15769–15774. https://doi.org/10.1073/pnas.1204357109.
51. Shakeel S, Dykeman EC, White SJ, Ora A, Cockburn JJB, Butcher SJ, Stockley PG, Twarock R. 2017. Genomic RNA folding mediates assembly of human parechovirus. Nat Commun 8:5. https://doi.org/10.1038/s41467-016-0011-z.
52. Patel N, White SJ, Thompson RF, Bingham R, Weiß EU, Maskell DP, Zlotnick A, Dykeman E, Tuma R, Twarock R, Ranson NA, Stockley PG. 2017. HBV RNA pre-genome encodes specific motifs that mediate interactions with the viral core protein that promote nucleocapsid assembly. Nat Microbiol 2:17098. https://doi.org/10.1038/nmicrobiol.2017.98.
53. Luque D, de la Escosura A, Snijder J, Brasch M, Burnley RJ, Koay MST, Carrascosa JL, Wuite GJL, Roos WH, Heck AJR, Cornelissen JJLM, Torres T, Castón JR. 2014. Self-assembly and characterization of small and monodisperse dye nanospheres in a protein cage. Chem Sci 5:575–581. https://doi.org/10.1039/C3SC52276H.
54. Beren C, Cui Y, Chakravarty A, Yang X, Rao ALN, Knobler CM, Zhou ZH, Gelbart WM. 2020. Genome organization and interaction with capsid protein in a multipartite RNA virus. Proc Natl Acad Sci U S A 117:10673–10680. https://doi.org/10.1073/pnas.1915078117.
55. Sarker S, Terron MC, Khandokar Y, Aragao D, Hardy JM, Radjainia M, Jimenez-Zaragoza M, de Pablo PJ, Coulibaly F, Luque D, Raidal SR, Forwood JK. 2016. Structural insights into the assembly and regulation of distinct viral capsid complexes. Nat Commun 7:13014. https://doi.org/10.1038/ncomms13014.
56. Luque D, Castón JR. 2020. Cryo-electron microscopy for the study of virus assembly. Nat Chem Biol 16:231–239. https://doi.org/10.1038/s41589-020-0477-1.
57. Luque D, Mata CP, Suzuki N, Ghabrial SA, Castón JR. 2018. Capsid structure of dsRNA fungal viruses. Viruses 10:481. https://doi.org/10.3390/v10090481.
58. Nakamichi Y, Miyazaki N, Tsutsumi K, Higashiura A, Narita H, Murata K, Nakagawa A. 2019. An assembly intermediate structure of rice dwarf virus reveals a hierarchical outer capsid shell assembly mechanism. Structure 27:439–448.E3. https://doi.org/10.1016/j.str.2018.10.029.
59. Jiménez-Zaragoza M, Yubero MP, Martín-Forero E, Castón JR, Reguera D, Luque D, de Pablo PJ, Rodríguez JM. 2018. Biophysical properties of single rotavirus particles account for the functions of protein shells in a multilayered virus. Elife 7:e37295. https://doi.org/10.7554/eLife.37295.
60. Hill CL, Booth TF, Prasad BV, Grimes JM, Mertens PP, Sutton GC, Stuart DI. 1999. The structure of a cypovirus and the functional organization of dsRNA viruses. Nat Struct Biol 6:565–568. https://doi.org/10.1038/9347.
61. Tang J, Naitow H, Gardner NA, Kolesar A, Tang L, Wickner RB, Johnson JE. 2005. The structural basis of recognition and removal of cellular mRNA 7-methyl G 'caps' by a viral capsid protein: a unique viral response to host defense. J Mol Recognit 18:158–168. https://doi.org/10.1002/jmr.724.
62. Fujimura T, Esteban R. 2011. Cap-snatching mechanism in yeast L-A double-stranded RNA virus. Proc Natl Acad Sci U S A 108:17667–17671. https://doi.org/10.1073/pnas.1111900108.
63. Tang J, Ochoa WF, Sinkovits RS, Poulos BT, Ghabrial SA, Lightner DV, Baker TS, Nibert ML. 2008. Infectious myonecrosis virus has a totivirus-like, 120-subunit capsid, but with fiber complexes at the fivefold axes. Proc Natl Acad Sci U S A 105:17526–17531. https://doi.org/10.1073/pnas.0806724105.
64. Nibert ML, Takagi Y. 2013. Fibers come and go: differences in cell-entry components among related dsRNA viruses. Curr Opin Virol 3:20–26. https://doi.org/10.1016/j.coviro.2012.10.006.
65. Okamoto K, Ferreira RJ, Larsson DSD, Maia F, Isawa H, Sawabe K, Murata K, Hajdu J, Iwasaki K, Kasson PM, Miyazaki N. 2020. Acquired functional capsid structures in metazoan totivirus-like dsRNA virus. Structure 28:888–896.E3. https://doi.org/10.1016/j.str.2020.04.016.
66. Liu H, Cheng L. 2015. Cryo-EM shows the polymerase structures and a nonspooled genome within a dsRNA virus. Science 349:1347–1350. https://doi.org/10.1126/science.aaa4938.
67. Zhang X, Ding K, Yu X, Chang W, Sun J, Zhou ZH. 2015. In situ structures of the segmented genome and RNA polymerase complex inside a dsRNA virus. Nature 527:531–534. https://doi.org/10.1038/nature15767.
68. Sato Y, Castón JR, Suzuki N. 2018. The biological attributes, genome architecture and packaging of diverse multi-component fungal viruses. Curr Opin Virol 33:55–65. https://doi.org/10.1016/j.coviro.2018.07.009.
69. Medrano M, Valbuena A, Rodriguez-Huete A, Mateu MG. 2019. Structural determinants of mechanical resistance against breakage of a virus-based protein nanoparticle at a resolution of single amino acids. Nanoscale 11:9369–9383. https://doi.org/10.1039/c9nr01935a.
70. Guerra P, Valbuena A, Querol-Audi J, Silva C, Castellanos M, Rodríguez-Huete A, Garriga D, Mateu MG, Verdaguer N. 2017. Structural basis for biologically relevant mechanical stiffening of a virus capsid by cavity-creating or spacefilling mutations. Sci Rep 7:4101. https://doi.org/10.1038/s41598-017-04345-w.
71. Hernando-Pérez M, Miranda R, Aznar M, Carrascosa JL, Schaap IA, Reguera D, de Pablo PJ. 2012. Direct measurement of phage phi29 stiffness provides evidence of internal pressure. Small 8:2366–2370. https://doi.org/10.1002/smll.201200664.
72. Shevchenko A, Jensen ON, Podtelejnikov AV, Sagliocco F, Wilm M, Vorm O, Mortensen P, Shevchenko A, Boucherie H, Mann M. 1996. Linking genome and proteome by mass spectrometry: large-scale identification of yeast proteins from two dimensional gels. Proc Natl Acad Sci U S A 93:14440–14445. https://doi.org/10.1073/pnas.93.25.14440.
73. Ruiz-Ruiz S, Sánchez-Carrillo S, Ciordia S, Mena MC, Méndez-Garcia C, Rojo D, Bargiela R, Zubeldia-Varela E, Martínez-Martínez M, Barbas C, Ferrer M, Moya A. 2020. Functional microbiome deficits associated with ageing: chronological age threshold. Aging Cell 19:e13063. https://doi.org/10.1111/acel.13063.
74. McClure R, Balasubramanian D, Sun Y, Bobrovskyy M, Sumby P, Genco CA, Vanderpool CK, Tjaden B. 2013. Computational analysis of bacterial RNA-Seq data. Nucleic Acids Res 41:e140. https://doi.org/10.1093/nar/gkt444.
75. Tjaden B. 2015. De novo assembly of bacterial transcriptomes from RNA-seq data. Genome Biol 16:1. https://doi.org/10.1186/s13059-014-0572-2.
76. Magoc T, Wood D, Salzberg SL. 2013. EDGE-pro: estimated degree of gene expression in prokaryotic genomes. Evol Bioinform Online 9:127–136. https://doi.org/10.4137/EBO.S11250.
77. Ortega-Esteban A, Horcas I, Hernando-Perez M, Ares P, Perez-Berna AJ,

San Martin C, Carrascosa JL, de Pablo PJ, Gomez-Herrero J. 2012. Minimizing tip-sample forces in jumping mode atomic force microscopy in liquid. Ultramicroscopy 114:56–61. https://doi.org/10.1016/j.ultramic.2012.01.007.
78. Sader JE, Chon JWM, Mulvaney P. 1999. Calibration of rectangular atomic force microscope cantilevers. Rev Sci Instrum 70:3967–3969. https://doi.org/10.1063/1.1150021.
79. Horcas I, Fernandez R, Gomez-Rodriguez JM, Colchero J, Gomez-Herrero J, Baro AM. 2007. WSXM: a software for scanning probe microscopy and a tool for nanotechnology. Rev Sci Instrum 78:013705. https://doi.org/10.1063/1.2432410.
80. Zheng SQ, Palovcak E, Armache JP, Verba KA, Cheng Y, Agard DA. 2017. MotionCor2: anisotropic correction of beam-induced motion for improved cryo-electron microscopy. Nat Methods 14:331–332. https://doi.org/10.1038/nmeth.4193.
81. Rohou A, Grigorieff N. 2015. CTFFIND4: fast and accurate defocus estimation from electron micrographs. J Struct Biol 192:216–221. https://doi.org/10.1016/j.jsb.2015.08.008.
82. Scheres SH. 2012. RELION: implementation of a Bayesian approach to cryo-EM structure determination. J Struct Biol 180:519–530. https://doi.org/10.1016/j.jsb.2012.09.006.
83. de la Rosa-Trevín JM, Quintana A, Del Cano L, Zaldivar A, Foche I, Gutiérrez J, Gómez-Blanco J, Burguet-Castell J, Cuenca-Alba J, Abrishami V, Vargas J, Oton J, Sharov G, Vilas JL, Navas J, Conesa P, Kazemi M, Marabini R, Sorzano CO, Carazo JM. 2016. Scipion: a software framework toward integration, reproducibility and validation in 3D electron microscopy. J Struct Biol 195:93–99. https://doi.org/10.1016/j.jsb.2016.04.010.
84. Vilas JL, Tagare HD, Vargas J, Carazo JM, Sorzano COS. 2020. Measuring local-directional resolution and local anisotropy in cryo-EM maps. Nat Commun 11:55. https://doi.org/10.1038/s41467-019-13742-w.
85. Huang CC, Meng EC, Morris JH, Pettersen EF, Ferrin TE. 2014. Enhancing UCSF Chimera through web services. Nucleic Acids Res 42:W478–W484. https://doi.org/10.1093/nar/gku377.
86. Brown A, Long F, Nicholls RA, Toots J, Emsley P, Murshudov G. 2015. Tools for macromolecular model building and refinement into electron cryo-microscopy reconstructions. Acta Crystallogr D Biol Crystallogr 71:136–153. https://doi.org/10.1107/S1399004714021683.
87. Adams PD, Afonine PV, Bunkoczi G, Chen VB, Davis IW, Echols N, Headd JJ, Hung LW, Kapral GJ, Grosse-Kunstleve RW, McCoy AJ, Moriarty NW, Oeffner R, Read RJ, Richardson DC, Richardson JS, Terwilliger TC, Zwart PH. 2010. PHENIX: a comprehensive Python-based system for macromolecular structure solution. Acta Crystallogr D Biol Crystallogr 66:213–221. https://doi.org/10.1107/S0907444909052925.
88. Chen VB, Arendall WB, 3rd, Headd JJ, Keedy DA, Immormino RM, Kapral GJ, Murray LW, Richardson JS, Richardson DC. 2010. MolProbity: all-atom structure validation for macromolecular crystallography. Acta Crystallogr D Biol Crystallogr 66:12–21. https://doi.org/10.1107/S0907444909042073.
89. Pettersen EF, Goddard TD, Huang CC, Couch GS, Greenblatt DM, Meng EC, Ferrin TE. 2004. UCSF Chimera—a visualization system for exploratory research and analysis. J Comput Chem 25:1605–1612. https://doi.org/10.1002/jcc.20084.